

Dynamical Schwinger effect and non-perturbative light detection in lead halide perovskites

Dusan Lorenc,^{1,*} Artem G. Volosniev,^{1,2,*} Ayan A. Zhumekenov,^{3,†} Seungho Lee,¹ Maria Ibáñez,¹ Osman M. Bakr,³ Mikhail Lemeshko,¹ and Zhanybek Alpichshev^{1,‡}

¹*ISTA (Institute of Science and Technology Austria), Am Campus 1, 3400 Klosterneuburg, Austria*

²*Department of Physics and Astronomy, Aarhus University, Ny Munkegade 120, DK-8000 Aarhus, Denmark*

³*KAUST (King Abdullah University of Science and Technology), Thuwal 23955, Saudi Arabia*

Dielectric breakdown of physical vacuum (Schwinger effect) is the textbook demonstration of compatibility of Relativity and Quantum theory. Although, the observation of this effect in its original static formulation is practically unachievable, it has been shown that the requirements on field strengths can be significantly reduced for dynamical generalizations of Schwinger effect. Here, we report on observation of an analog dynamical Schwinger effect in gapped Dirac semiconductor lead-halide perovskite MAPbBr₃. Specifically, we observe strong photoluminescence of a lead-halide perovskite driven by deep sub-gap irradiation, and use the quasi-adiabatic Landau-Dykhne approach to interpret our data in terms of the dynamical Schwinger effect. Further, the exponential sensitivity of the Schwinger effect to driving fields allows us to measure the local frozen-in fields in a nominally cubic single perovskite crystal at room temperature. Finally, we demonstrate an AC analogue of biasing in our system – the non-perturbative cooperation between two time-dependent fields simultaneously driving the sample. Our results establish lead-halide perovskites as an excellent platform for simulating effects of strong fields on Dirac fields. In addition, they contribute to the on-going discussion about inversion-breaking in MAPbBr₃ single crystal and pave the way for a mid-infrared light detection with lead-halide perovskites.

I. INTRODUCTION

One of the most important insights coming from the synthesis of Quantum Mechanics and Special Relativity is the realization that vacuum is not empty. Instead, it is rather a fluctuating sea of virtual particle-antiparticle pairs, which can be in principle made real in the presence of external fields [1]. However, this process is negligible unless the fields are of the order of $E_S \approx 10^{20}$ V/m at which point particle-antiparticle creation leads to the dielectric breakdown of vacuum. In view of the enormity of E_S and its intuitive interpretation as the maximal static electric field attainable in principle, it is natural that the actual attempts to realize vacuum breakdown (“Schwinger Effect”, SE) focus on its dynamical versions where the vacuum pair creation is achieved under the influence of time-dependent fields [2]. The experimental progress is motivated by a number of theoretical works that suggest to reduce the field amplitudes needed for the observation of SE by crafting profiles of the driving fields [3–5]. However, any theoretical proposal must rely on certain simplifying assumptions, which due to the inherently non-perturbative character of SE may be decisive to the outcome [6, 7]. Given that current technology is not capable to test these ideas in practice, it is hard to tell at the moment how realistic will they ultimately turn out to be.

In this context it appears desirable to be able to simulate the Schwinger effect and the various approaches to it in a more accessible setting. An obvious direction is a realization of field-induced tunneling ionization in a semiconductor with a Dirac-like band dispersion. It is straightforward to demonstrate then that the threshold field in this case would be $E_s \sim \Delta/ea \sim 10^9$ V/m [8], which is readily achievable in modern laboratories (here Δ , a and e are the band gap, unit lattice length and the elementary charge, respectively). However, it turns out that the observation of this scaled-down version of SE also poses significant challenges. The main difficulty here lies in the fact that despite an abundance of far-reaching analogies [9], there is an important difference between the “true” Dirac field in vacuum and a Dirac material in that the former features relativistic invariance while the latter does not. The important consequence in question is that a free particle in vacuum can in principle be accelerated indefinitely, while a charge carrier in a semiconductor can produce secondary particles once it acquires a certain threshold kinetic energy comparable to the band-gap [10]. Since the threshold for this process $E_{av} \sim \Delta/e\lambda_{mfp}$ is significantly lower than that for tunneling ionization (here $\lambda_{mfp} > a$ is the mean free path of charged carriers in the material), the population of secondary charge carriers will tend to dominate over tunnel-ionized carriers, often ending up in a catastrophic avalanche breakdown of the material. As a result of these complications, the observations of tunneling ionization have been limited so far either to the cases where the relevant tunneling region is restricted to a narrow part of space to avoid avalanche breakdown (e.g. tunneling ionization in single atoms [11] or tunnel diodes [12] and tunnel junctions [13, 14] in electronics); or to extended

* These authors contributed equally

† Present address: School of Materials Science and Engineering (MSE), Nanyang Technological University, Singapore 639798

‡ alpishhev@ist.ac.at

systems with no gap [15]. However, to establish a direct connection to the efforts in high energy physics, it is necessary to realize an analog Schwinger effect in an extended Dirac material with a finite bandgap.

In this Article, we report the observation of dynamical tunneling ionization in a single-crystal sample of lead halide perovskite (LHP), which realizes a gapped Dirac system [16]. In order to suppress avalanche formation and emphasize tunneling, we note that the former needs a finite amount of time to build up while the latter occurs quasi-instantaneously. Therefore, we seek to induce ionization with alternating electric fields using frequencies that, on the one hand, correspond to photon energies significantly smaller than the band gap $\hbar\omega \ll \Delta$ (to ensure that we operate in the quasi-adiabatic regime); on the other hand, they should oscillate fast enough to avoid an avalanche breakdown ($\omega \gtrsim eE/\sqrt{m\Delta}$, where E and m are the magnitude of the applied electric field and the band mass of the charge carrier, respectively). Additionally, we are careful to keep our irradiation intensity levels well below impact ionization thresholds for our pulse durations $\tau \approx 300\text{fs}$ to suppress the population of secondary charge carriers [17]. Operation with relatively small intensities also allows us to avoid ‘memory’ effects in our system, which are extrinsic to tunneling ionization (see Supplementary Material). This is necessary to reveal the tunneling processes inherent in the material and also to be able to describe them using quasi-adiabatic methods.

Low irradiation intensities, however, imply that all measurements need to be performed in the regime where the concentration of tunnel-induced carriers is so low that standard transport measurements cannot be used for studying tunnel ionization. Therefore, our approach here is to infer the population of photo-excited carriers from the intensity of photoluminescence (PL) emitted upon their recombination with each other. The success of this approach crucially depends on two factors. First, the energy gap of the material should be free of defects to enhance the probability of tunneling directly into the conduction band. Second, the parent material should enjoy high photoluminescence quantum efficiency, namely the ratio of radiative recombinations to the total number of excitations [18]. These considerations are the primary motivation for the choice of lead halide perovskites as the base for realizing the solid-state version of SE [19]. Furthermore, effective behavior of lead halide perovskites renowned for excellent quantum optoelectronic properties [20] is described very accurately by a Dirac equation with a non-zero mass [21–23], strengthening the analogy between our findings and the physics of SE.

II. OBSERVATION OF DYNAMICAL SCHWINGER EFFECT IN MAPbBr₃

Lead-halide perovskites are known to feature strong sub-bandgap response in terms of two- and three-photon adsorption [24, 25] whose analysis has been mainly fo-

cused around the photophysical properties of LHPs in the near-infrared regime as it can shed light onto surprising solar cell (photovoltaic) performance of LHPs [26]. At the same time, the response of the system to photons with lower frequency remains largely unexplored. In Fig. 1C we show the PL spectrum of MAPbBr₃ illuminated with mid-infrared radiation ($\lambda \approx 4\mu\text{m}$). Given the wavelength of PL ($\lambda_{\text{PL}} \approx 570\text{nm}$) which roughly corresponds to the bandgap energy in MAPbBr₃ ($\Delta \approx 2.3\text{eV}$ [27, 28]) this process corresponds to a whopping frequency conversion factor of ~ 10 at the face value. Combined with the exponential sensitivity of this process to the intensity of the irradiating field in Fig. 1D, we are compelled to rationalize the observed PL under deep sub-gap irradiation as quasi-adiabatic tunnel ionization of electrons across the semiconductor band gap using the standard terminology of strong-field phenomena [29] (similar behavior was observed in CsPbBr₃, which indicates the general character of the phenomenon; see Supplementary Material and Ref. [30]). This observation comprises the central finding of this work. In the following we will further substantiate this qualitative observation by a quantitative analysis of ionization in a periodically driven Dirac-like band structure.

A. Quasi-adiabatic tunneling

Tunneling is the quintessential quantum effect whereby a system undergoes a transition that can be described semi-classically by a trajectory of which at least a part passes through a classically-forbidden region in the parameter space. As a result the rate of this transition is strongly suppressed, being exponentially sensitive to the width of the classically-forbidden region [31], see Fig. 1A. For instance, in a static electric field, E , the rate of tunneling ionization W across the gap Δ can be shown to be

$$W \propto \exp(-E_s/|E|) \quad (1)$$

with the characteristic cut-off field introduced above $E_s \sim \Delta/ea$ [1, 32, 33]. A convenient way to extend this limiting expression to the problem of tunneling excitation of a semiconductor under the influence of time-dependent fields varying at the characteristic frequencies much smaller than those given by the bandgap is the so-called quasi-adiabatic Landau-Dykhne method [34]. Within this approach the ionization rate W can be shown (see Methods) to be given as

$$W \sim \exp(-2f(\gamma_K)\Delta/\omega), \quad (2)$$

where $f(x) = \text{arsinh}(x) - (\sinh(2\text{arsinh}(x)) - 2\text{arsinh}(x))/(8x^2)$, and γ_K is the so-called Keldysh parameter of the problem whose numeric value depends on the strength and the frequency of the driving field as well as on the details of the band structure of the material in question [35]. In the specific case of

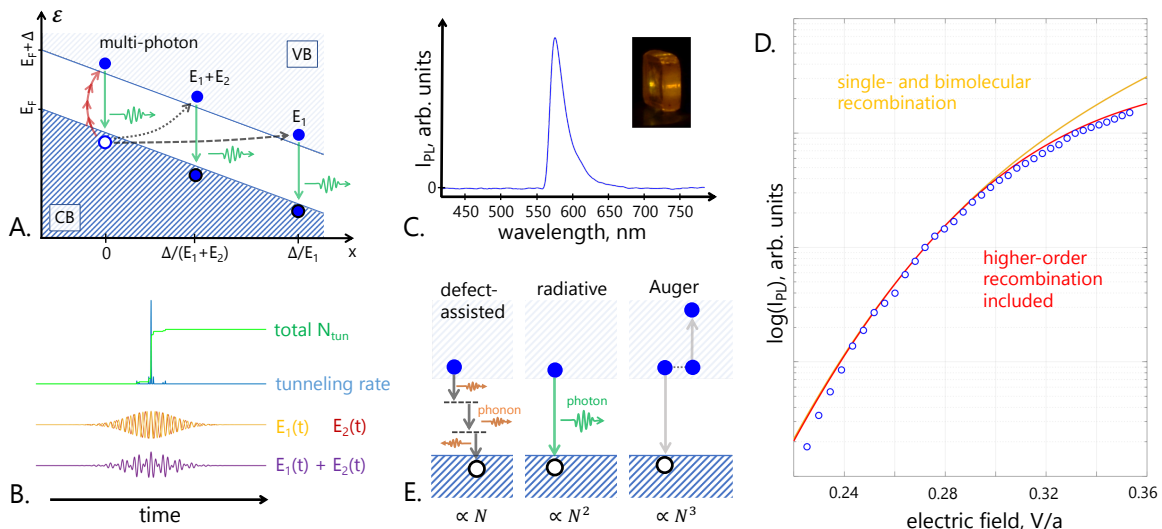


FIG. 1. A) Schematic diagram of ionization across the energy gap Δ due to multiphoton process, and due to tunneling under the influence of different applied field amplitudes (E_1 and $E_1 + E_2$). It can be seen that the magnitude of E determines the width of the forbidden range, thus affecting the net tunneling rate exponentially (see the text for details); B) Tunneling under the influence of the of alternating fields $E_1(t)$ and $E_2(t)$ (yellow and red); due to exponential sensitivity of the tunneling rate (blue) on the magnitude of the field, the tunneling rate peaks at the maximum of the total field (magenta); consequently the total number of transitions (green) depends only on the sum of the amplitudes of applied time-dependent fields; C) PL spectrum of MAPbBr₃ single crystal sample pumped by $\lambda = 4\mu\text{m}$ radiation; *Inset*: MAPbBr₃ crystal with PL coming from the bulk of the sample; D) PL spectra under $\lambda = 4\mu\text{m}$ pumping, together with our theoretical prediction for weak fields (no fit parameters), and for intermediate electric fields (see the text for details). Note that we normalize all curves to be unity at a given value of the field ($eaE_{AC} \simeq 0.272\text{eV}$), for convenience. E) An illustration of several most common channels of photo-carrier recombination with characteristic rate dependencies on the total number of charge carriers (bottom).

lead-bromide perovskites, density functional theory calculations provide $\gamma_K \simeq 0.85\hbar\omega/(eaE_{AC})$, where E_{AC} is the strength of the electric field induced by the laser, and $a \simeq 0.586\text{nm}$ is the lattice constant MAPbBr₃ in cubic phase [21].

The value of the Keldysh parameter determines the degree of adiabaticity of the problem, the two limiting cases being pure adiabatic tunneling [36] ($\gamma_K \rightarrow 0$) and multiphoton absorption ($\gamma_K \rightarrow \infty$) as illustrated in Fig. 1A. In our experiment $\gamma_K \lesssim 1$ (see Fig. 1D), which puts us in the quasi-adiabatic tunneling regime, where the tunneling rate can be well approximated by $W \sim \exp[-1.4\Delta/(eaE_{AC})]$ exhibiting the exponential dependence on the external electric field characteristic of the non-perturbative tunneling processes such as (static) Schwinger effect [cf. Eq. (1)].

B. Comparison to the experiment

In this section we confirm the tunneling nature of the ionization by deriving the functional dependence of the PL intensity, I_{PL} , on the strength of the pumping mid-infrared (mid-IR) radiation. Naively, one might assume $I_{PL} \propto W$, i.e., every single tunneling event results in a PL photon. However this is only true if: 1) there are no non-radiative recombination channels; 2) the photo-excited electron-hole pairs remain well-separated in space; 3) the

density of charge carriers is low. Neither of these conditions are satisfied in our experiment. First of all, despite the excellent photoelectronic properties of LHPs the non-radiative recombination processes in them cannot be ignored altogether. Similarly, the long diffusion lengths of photocarriers in LHPs imply strong overlap between electron-hole pairs, which gives rise to a bi-molecular character of the recombination processes [37, 38].

In view of the discussion above, to quantitatively describe the photoluminescence in perovskites, one needs to know the population dynamics of photoexcitations $n(t)$ from which one can calculate the PL intensity based upon the bi-molecular recombination in lead halide perovskites, $I_{PL} \sim \int_0^t n(t)^2 dt$. The general equation governing the population of charge carriers $n(t)$ can be written as:

$$-dn(t)/dt = A_1 n + A_2 n^2 + A_3 n^3 + \dots \quad (3)$$

Here, the coefficients $\{A_i\}$ describe the rates of different decay channels of $n(t)$ such as: defect-assisted (A_1), bi-molecular (both radiative- and non-radiative; A_2), and Auger-type (A_3) recombination processes followed by higher-order processes, which should, in principle, be taken into account for sufficiently high densities of charge carriers, see Fig. 1E.

In the limit of weak pumping fields, $n(t)$ remains small at all times, implying that $n(t) = n(0) \exp(-A_1 t)$ and

$I_{PL} \sim n(0)^2$ where the initial population $n(0)$ is proportional to the tunneling ionization rate W . This result is accurate as long as $n_0 \ll A_1/A_2$. Note that $A_1/A_2 \simeq 3.5 \times 10^{16} \text{cm}^{-3}$ [37]. As the pumping intensity grows, the omission of higher-order terms in Eq. (3) is no longer justified. For example, the inclusion of both mono- and bi-molecular channels leads to $I_{PL} \sim \alpha W - \ln(1 + \alpha W)$, where α is a fitting parameter (see Methods). This expression is accurate for $eaE_{AC} \lesssim 0.3\text{eV}$, providing an estimate for a number of excited particles in the system $10^{16} - 10^{17} \text{cm}^{-3}$ at this field. For higher excitation densities, the channels beyond bi-molecular recombination have to be included.

In Fig. 1D we show the results of the fit limited to second (bi-molecular) processes (yellow curve) as well a phenomenological fit including higher-order channels (red curve) line. The phenomenological fit is motivated by our analytical results. It has the form $I_{PL} \sim \alpha \tilde{W} - \ln(1 + \alpha \tilde{W})$, where $\tilde{W} = W/(1 + \beta W)$ is a renormalized ionization rate that takes into account that for large densities only a fraction of charge carriers can recombine radiatively. Note that the phenomenological fit has now two parameters α and β . The overall prefactor that connects I_{PL} to n^2 is beyond the Landau-Dykhne approach. One could in principle introduce this prefactor as another fit parameter. We refrain from doing so by properly normalizing the data, see Fig. 1D.

III. DISCUSSION

The inherent non-perturbative character of tunneling implies non-trivial cooperation between various fields simultaneously driving a system. The basic intuition here can be inferred already from the expression in Eq. (1), which suggests that the overwhelming majority of tunneling events occurs near the moment of time t_0 when the total field $E_{tot}(t)$ reaches its maximum $E_{tot}(t_0) = E_{max}$, see Fig. 1B. For instance, in the case of tunneling under the simultaneous influence of two slowly changing electric fields $E_1(t) = E_1 \cos(\omega_1 t)$, and $E_2(t) = E_2 \cos(\omega_2 t + \phi)$, the total number of transitions according to this logic is expected to be $N_{tot} = \int W(t) dt \propto \exp(-E_0/(|E_1| + |E_2|))$ (see Fig. 1B). While this simple example is valid only for $\omega_1, \omega_2 \rightarrow 0$ it in fact illustrates the more general phenomenon of exponential cooperative enhancement of tunneling yield. A more rigorous treatment of this effect can be provided within the quasi-adiabatic formalism [39]. Below, we illustrate that the exponential cooperative enhancement can be used a valuable resource.

A. Tunneling enhancement in LHP due to local frozen-in electric fields.

The distinctive exponential sensitivity of tunneling ionization rate on the peak value of the *net* applied field

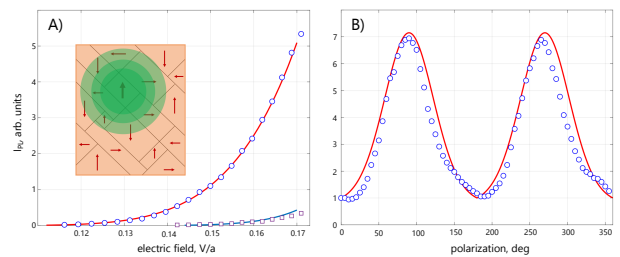


FIG. 2. A) PL as a function of the applied electric field for two orthogonal polarization orientations aligned with the crystal axes of MAPbBr₃ (markers). The corresponding fits according to our model to the data are presented as solid curves. The inset shows a cartoon of MAPbBr₃ with hypothetical ferroelectric domains overlaid with a schematic representation of the irradiating laser spot whose diameter is $d \approx 200 \mu\text{m}$ ($1/e^2$); B) Polarization scan taken at a fixed value of the external electric field $eaE_{AC} \simeq 0.180\text{eV}$.

can be used as a resource to detect weak local fields in a material. This can be best illustrated in the quasi-static regime describe above. Using the Landau-Dykhne approach it can also be demonstrated in a general case that even a weak static frozen-in field E_1 ($\omega_1 = 0$) can strongly enhance the tunneling rate W due to the additional driving field $E_2(t)$ (see Supplementary Material). The fact that local fields can enhance PL yield is consistent with a qualitative observation that we see stronger PL in the vicinity of structural defects (edges, surfaces) of LHPs where internal electric fields, E_1 , are expected to appear [40].

As an application of this sensitivity of PL to E_1 we will use it to study the highly debated frozen-in electric fields E_{DC} in LHPs [41], which lead to a broken inversion symmetry even for nominally cubic lead-halide perovskites. It is worth noting here that the method merits certain advantages as compared to some of the conventional techniques for detecting local breaking of inversion symmetry such as second-harmonic generation or angle-resolved photoemission. First of all, our method is not confined to the vicinity of the sample surface since the used electric fields have sub-gap frequencies and hence can penetrate the sample. Second, the peculiarity of tunneling is that it is sensitive to the *absolute value* of field amplitudes, cf. Eq. (1). Therefore there is a finite net effect due to local inversion breaking even if the local fields spatially average to zero. Finally, another implication of the field cooperation is that PL should strongly depend on the polarization of the external field.

For experimental validation, we measure PL from a single-crystal MAPbBr₃ as a function of intensity of the driving mid-infrared $\lambda = 4 \mu\text{m}$ radiation. The resulting dependence plotted in Fig. 2A indicates that the tunneling ionization efficiency depends strongly on the polarization of the pumping field. To elucidate the nature of this polarization dependence, we scan PL as a function of polarization at a fixed pump intensity as shown in Fig. 2B.

The two-fold symmetric polarization dependence in Fig. 2B might appear surprising since this measurement was performed at room temperature where MAPbBr₃ is expected to be in the cubic phase, i.e., four-fold symmetric (e.g., consider the two-photon absorption experiments like in Ref. [42]). The data in Fig. 2B therefore indicates an unexpected lowering of symmetry in MAPbBr₃ in the nominally cubic phase. In the most straightforward explanation this could be attributed to an extrinsic factor such as residual stress in the crystal structure that would lift the four-fold symmetry of the electronic band structure. However it can be demonstrated that, that in this case in order to reproduce the magnitude of the effect in Fig. 2 the intrinsic strains in the system have to reach relatively large ($\simeq 0.5\%$) levels [43], which are not expected in a single-crystal LHP [44] (see Supplementary Material for more details).

In an alternative scenario, the observed anisotropy can be attributed to the local frozen-in electric fields, that were conjectured to be present in lead-halide perovskites [40, 45]. Indeed the exponential sensitivity of PL on applied fields implies that one can obtain the anisotropy observed in Fig. 2 already with moderate static fields. In Figs. 2A and B we show that all of the experimental data can be reproduced within the two-field Landau-Dykhne formalism presented in the Supplementary Material. Based on the fitting, we estimate the numeric value for the internal static fields in room-temperature single-crystal MAPbBr₃ to be of the order of $E_{DC} \sim 0.1\text{V/nm}$. Within this interpretation of the PL anisotropy, the PL gets maximum enhancement when the polarization of the driving optical field coincides with the direction of E_{DC} . That this direction happens to be aligned with direction of Pb-Br bonds ([001] of the cubic lattice) is consistent with previous observations of possible ferroelectricity in MAPbI₃ [46, 47]. Note that Fig. 1D is produced using electric fields that are stronger than those presented in Fig. 2A. Further, we rotated the polarization of the external electric field to have minimal PL intensity. This allowed us to minimize the effect of the frozen-in electric fields in the data demonstrated in Fig. 1D.

Importantly, we also observe that the two-fold symmetric pattern of PL is subject to the spatial extent of the focal spot of the driving laser. Namely, we observe that that the two-fold symmetry in Fig. 2 is only present for sufficiently focused beams. For larger illumination spots, the pattern turns out to be four-fold symmetric (see Supplementary Material). This can be naturally explained if more than one ferroelectric domain with different field directions participate in the fluorescence process. This interpretation agrees well with the previous estimations of the size of possible ferroelectric domains of several microns in MAPbI₃ [45, 48].

B. Cooperation of dynamic fields and AC-biasing

The hallmark feature of quantum tunneling is its exponential sensitivity to external parameters, which has enabled applications defying the classical common sense. The most celebrated example is the scanning tunneling microprobes where exponential sensitivity of the tunneling current means that the overwhelming majority of it is flowing through the single atom that happens to stick out the most toward the sample [14, 49]. Realization of this has led to unprecedented sub-atom-scale spatial resolutions. Other celebrated applications of tunneling-related process include the tunnel diode [50] with its unique I-V characteristics and high-harmonic generation in atomic optics where deeply sub-threshold laser light promotes electrons in an atom to unoccupied states [51], thus initializing the process of extreme frequency conversion of radiation.

Likewise, besides being a fascinating example of quantum tunneling dynamics, our findings are also of practical importance. Indeed the cooperation effect discussed in the previous section implies that the total yield of tunneling ionization across the band gap driven by an AC-field can be significantly enhanced in the presence of an additional “boosting” AC-field, which does not have to be in any particular phase or frequency relationship to the first field. In order to demonstrate this “AC-biasing” phenomenon, we measure the PL from the MAPbBr₃ sample irradiated by a $4.5\mu\text{m}$ beam while it is being “AC-biased” by an additional $1\mu\text{m}$ beam.

In Fig. 3A we show the cumulative PL coming from the sample as a function of the delay time between the two pulses in cross- and parallel polarization geometries (yellow x- and blue o-markers, respectively). As can be clearly seen, the PL signal is enhanced only when the two pulses of the same polarization overlap in time, i.e., when the amplitude of the sum field is maximized in full agreement with the concept of the dynamical assistance in quantum tunneling introduced at the beginning of this section. As a further illustration of the same phenomenon, we present in Fig. 3(B-D) the 2D dependence of PL on the intensity of each infrared beam.

As a demonstration of the practical use of this effect, we present in Fig. 3E the effect of AC-biasing on PL produced by a mid-infrared beam ($4.5\mu\text{m}$) in MAPbBr₃ biased with $1\mu\text{m}$ radiation at $I_{\text{bias}} = 5 \times 10^{13}\text{W/m}^2$. Here, we show the differential photoluminescence for two beams $\Delta PL(I) = PL(I_1, I_{\text{bias}}) - PL(I_1, 0) - PL(0, I_{\text{bias}})$, where $PL(I_1, I_{\text{bias}})$ stands for the total PL emitted by the sample when irradiated by mid- and near-infrared pulses overlapping in time. As can be seen the differential sensitivity of PL can be made linear in the intensity of the mid-IR which opens broad possibilities for efficient mid-infrared sensors based upon lead-halide perovskites. We demonstrate the latter by overlapping the two beams (mid- and near-infrared) on a screen covered by LHP microparticles. As can be seen in Fig. 3F-G, there is clear enhancement in local PL from the region of spatial over-

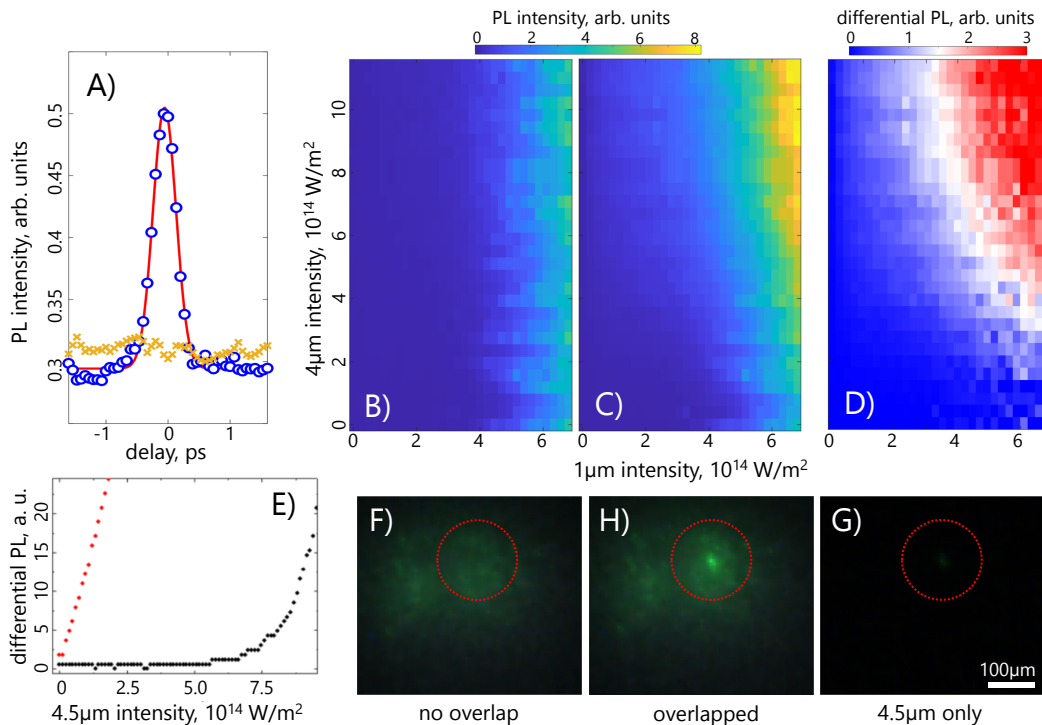


FIG. 3. A) Cumulative PL from single-crystal MAPbBr₃ as a function of the time delay between 1 μ m and 4 μ m pulses with parallel- (blue circles) and orthogonal (yellow crosses) polarizations; solid red line is a Gaussian fit to the curve used as the guide to an eye; B)-D) Two-color experiment on single-crystal MAPbBr₃: cumulative PL as a function of the intensities of 1 μ m and 4 μ m with $\delta t = 7$ ps (“off” position, panel B) and overlapped in time (“on” position, panel C) and the differential PL defined as the difference between “on”- and “off”-positions (panel D); E) Differential PL as a function of mid-infrared intensity (4.5 μ m) biased with 1 μ m at $I_{\text{bias}} = 5 \times 10^{13}$ W/m²; F)-H) Spatial profile of AC-biasing in an abraded sample of MAPbBr₃ (see Supplementary Material): spatial profile of cumulative PL with 1 μ m and 4.5 μ m pulses not overlapped- (panel F) and overlapped in time (panel H); G) PL produced by the pulse 4.5 μ m alone; red circle in F)-G) marks the position of the 4.5 μ m light beam.

lap. Curiously, due to the nonlinear sensitivity of PL on the pumping beam intensity, the apparent size of the overlap spot is significantly smaller (11 μ m) than the actual spot size of the mid-infrared pulse (160 μ m), which can be employed for super-resolution microscopy.

IV. SUMMARY

To summarize, we have demonstrated dynamical Schwinger effect in a Dirac semiconductor (lead-halide perovskite) and quantitatively described it with the quasi-adiabatic Landau-Dykhne approach. Further, we have employed the characteristic exponential sensitivity of tunneling ionization on driving fields to measure the local frozen-in fields in the nominally cubic MAPbBr₃ single crystal at room temperature contributing to the on-

going debate on the state of ferroelectricity in lead-halide perovskites. Finally, we have investigated the cooperation between two time-dependent fields simultaneously driving tunneling ionization and demonstrated that this cooperation can act as an AC analogue of biasing for an optical frequency upconversion. These findings pave the way for a mid-infrared light detection with lead-halide perovskites.

Acknowledgements A. G. V. thanks Peter Balling for useful discussions.

[1] J. Schwinger, *Physical Review* **82**, 664–679 (1951).
 [2] G. A. Mourou, T. Tajima, and S. V. Bulanov, *Rev. Mod. Phys.* **78**, 309 (2006).

[3] V. S. Popov, *JETP Lett.* **13**, 261 (1971).
 [4] A. Ringwald, *Physics Letters B* **510**, 107–116 (2001).
 [5] R. Schützhold, H. Gies, and G. Dunne, *Physical Review*

- Letters **101**, 130404 (2008).
- [6] H. Gies and K. Klingmüller, Phys. Rev. D **72**, 065001 (2005).
- [7] G. Torgrimsson, C. Schneider, J. Oertel, and R. Schützhold, Journal of High Energy Physics **2017**, 43 (2017).
- [8] M. F. Linder, A. Lorke, and R. Schützhold, Phys. Rev. B **97**, 035203 (2018).
- [9] T. Wehling, A. Black-Schaffer, and A. Balatsky, Advances in Physics **63**, 1 (2014).
- [10] D. Jena, *Quantum physics of semiconductor materials and devices* (Oxford University Press, 2022).
- [11] Y. P. Raizer, *Gas Discharge Physics* (Springer Berlin, Heidelberg, 1991).
- [12] L. Esaki, Phys. Rev. **109**, 603 (1958).
- [13] I. Giaever and K. Megerle, Physical Review **122**, 1101–1111 (1961).
- [14] C. J. Chen, *Introduction to Scanning Tunneling Microscopy* (Oxford University Press Oxford, 2007).
- [15] A. I. Berdyugin, N. Xin, H. Gao, S. Slizovskiy, Z. Dong, S. Bhattacharjee, P. Kumaravadivel, S. Xu, L. A. Ponomarenko, M. Holwill, D. A. Bandurin, M. Kim, Y. Cao, M. T. Greenaway, K. S. Novoselov, I. V. Grigorieva, K. Watanabe, T. Taniguchi, V. I. Fal'ko, L. S. Levitov, R. K. Kumar, and A. K. Geim, Science **375**, 430 (2022).
- [16] H. Jin, J. Im, and A. J. Freeman, Phys. Rev. B **86**, 121102 (2012).
- [17] B. Rethfeld, D. S. Ivanov, M. E. Garcia, and S. I. Anisimov, Journal of Physics D: Applied Physics **50**, 193001 (2017).
- [18] S. E. Braslavsky, Pure and Applied Chemistry **79**, 293–465 (2007).
- [19] T. Kirchartz, J. A. Márquez, M. Stolterfoht, and T. Unold, Advanced Energy Materials **10**, 1904134 (2020).
- [20] K. P. Goetz, A. D. Taylor, F. Paulus, and Y. Vaynzof, Advanced Functional Materials **30**, 1910004 (2020).
- [21] M. A. Becker, R. Vaxenburg, G. Nedelcu, P. C. Sercel, A. Shabaev, M. J. Mehl, J. G. Michopoulos, S. G. Lambrakos, N. Bernstein, J. L. Lyons, T. Stöferle, R. F. Mahrt, M. V. Kovalenko, D. J. Norris, G. Rainò, and A. L. Efros, Nature **553**, 189 (2018).
- [22] A. G. Volosniev, A. S. Kumar, D. Lorenc, Y. Ashourishokri, A. A. Zhumekenov, O. M. Bakr, M. Lemeshko, and Z. Alpichshev, Physical Review B **107**, 125201 (2023).
- [23] A. G. Volosniev, A. S. Kumar, D. Lorenc, Y. Ashourishokri, A. A. Zhumekenov, O. M. Bakr, M. Lemeshko, and Z. Alpichshev, Physical Review Letters **130**, 106901 (2023).
- [24] F. Zhou, X. Ran, D. Fan, S. Lu, and W. Ji, Advanced Optical Materials **9**, 2100292 (2021).
- [25] L. Mei, R. Huang, C. Shen, J. Hu, P. Wang, Z. Xu, Z. Huang, and L. Zhu, Advanced Optical Materials **10**, 2102656 (2022).
- [26] A. K. Jena, A. Kulkarni, and T. Miyasaka, Chemical Reviews **119**, 3036 (2019).
- [27] M. I. Saidaminov, A. L. Abdelhady, B. Murali, E. Alarousu, V. M. Burlakov, W. Peng, I. Dursun, L. Wang, Y. He, G. Maculan, A. Goriely, T. Wu, O. F. Mohammed, and O. M. Bakr, Nature Communications **6**, 7586 (2015).
- [28] J. Tilchin, D. N. Dirin, G. I. Maikov, A. Sashchiuk, M. V. Kovalenko, and E. Lifshitz, ACS Nano **10**, 6363–6371 (2016).
- [29] S. Y. Kruchinin, F. Krausz, and V. S. Yakovlev, Rev. Mod. Phys. **90**, 021002 (2018).
- [30] Z. Zhang, H. Ning, Z.-J. Liu, J. Hou, A. D. Mohite, E. Baldini, N. Gedik, and K. A. Nelson, “Keldysh tuning of photoluminescence in a lead halide perovskite crystal,” (2024), arXiv:2407.15253.
- [31] L. D. Landau and E. M. Lifshitz, *Quantum mechanics*, 3rd ed. (Butterworth-Heinemann, 1981).
- [32] F. Sauter, Zeitschrift für Physik **69**, 742–764 (1931).
- [33] C. Zener, Proceedings of the Royal Society of London. Series A, Containing Papers of a Mathematical and Physical Character **145**, 523 (1934).
- [34] N. B. Delone and V. P. Krainov, in *Multiphoton Processes in Atoms* (Springer Berlin Heidelberg, 2000) pp. 69–83.
- [35] L. V. Keldysh, Sov. Phys. JETP **20**, 1307 (1965).
- [36] Note that pure adiabatic tunneling competes with the avalanche breakdown. Indeed, the condition $\omega \gtrsim eE_{AC}/\sqrt{m\Delta} \simeq eaE_{AC}/\hbar$ is clearly violated in the limit $\gamma_K \rightarrow 0$. Here, we estimate $eE_{AC}/\sqrt{m\Delta}$ using parameters of MAPbBr₃.
- [37] J. M. Richter, M. Abdi-Jalebi, A. Sadhanala, M. Tabachnyk, J. P. Rivett, L. M. Pazos-Outón, K. C. Gödel, M. Price, F. Deschler, and R. H. Friend, Nature Communications **7**, 13941 (2016).
- [38] S. D. Stranks, ACS Energy Letters **2**, 1515 (2017).
- [39] A. M. Perelomov and V. S. Popov, Soviet Journal of Experimental and Theoretical Physics **25**, 336 (1967).
- [40] D. Niesner, M. Wilhelm, I. Levchuk, A. Osvet, S. Shrestha, M. Batentschuk, C. Brabec, and T. Fauster, Physical Review Letters **117**, 126401 (2016).
- [41] F. Ambrosio, F. D. Angelis, and A. R. Goñi, The Journal of Physical Chemistry Letters **13**, 7731 (2022).
- [42] X. Li, W. Liu, Y. Song, H. Long, K. Wang, B. Wang, and P. Lu, Nano Energy **68**, 104334 (2020).
- [43] Y. Chen, Y. Lei, Y. Li, Y. Yu, J. Cai, M.-H. Chiu, R. Rao, Y. Gu, C. Wang, W. Choi, H. Hu, C. Wang, Y. Li, J. Song, J. Zhang, B. Qi, M. Lin, Z. Zhang, A. E. Islam, B. Maruyama, S. Dayeh, L.-J. Li, K. Yang, Y.-H. Lo, and S. Xu, Nature **577**, 209–215 (2020).
- [44] Y. Li, H. Tian, N. Li, J. Guo, X. Ling, J. Yuan, J. Zhao, and Y. Deng, Crystal Growth & Design **24**, 4473–4480 (2024).
- [45] Y. Rakita, O. Bar-Elli, E. Meirzadeh, H. Kaslasi, Y. Peleg, G. Hodes, I. Lubomirsky, D. Oron, D. Ehre, and D. Cahen, Proceedings of the National Academy of Sciences **114**, E5504 (2017).
- [46] H. Röhm, T. Leonhard, M. J. Hoffmann, and A. Colmann, Advanced Functional Materials **30**, 1908657 (2019).
- [47] T. Leonhard, A. D. Schulz, H. Röhm, S. Wagner, F. J. Altermann, W. Rheinheimer, M. J. Hoffmann, and A. Colmann, Energy Technology **7**, 1800989 (2019).
- [48] M. U. Rothmann, W. Li, Y. Zhu, U. Bach, L. Spiccia, J. Etheridge, and Y.-B. Cheng, Nature Communications **8**, 14547 (2017).
- [49] G. Binnig, H. Rohrer, C. Gerber, and E. Weibel, Phys. Rev. Lett. **49**, 57 (1982).
- [50] L. Turner, ed., *Electronics Engineer's Reference Book* (Elsevier, 1976).
- [51] L. Yue and M. B. Gaarde, Journal of the Optical Society of America B **39**, 535 (2022).
- [52] K. Abiedh, Z. Zaaboub, and F. Hassen, Applied Physics A **127**, 623 (2021).

Methods

Sample preparation

Chemicals $\text{CH}_3\text{NH}_3\text{Br}$ (>99.99%) was purchased from GreatCell Solar Ltd. (formerly Dyesol) and used as received. PbBr_2 (98%), CsBr (99.9% trace metals basis), DMF (anhydrous, 99.8%), and DMSO (anhydrous, 99.9%) were purchased from Sigma Aldrich and used as received.

Synthesis of $\text{CH}_3\text{NH}_3\text{Br}_3/\text{CsPbBr}_3$ perovskite single crystals. A 1.5 M solution of $\text{CH}_3\text{NH}_3\text{Br}/\text{PbBr}_2$ in DMF was prepared, filtered through a 0.45 μm -pore-size PTFE filter; and the vial containing 0.5-1 ml of the solution was placed on a hot plate at 30 °C. Then the solution was gradually heated to 60 °C and kept at this temperature until the formation of $\text{CH}_3\text{NH}_3\text{Br}_3$ crystals. The crystals can be grown into larger sizes by elevating the temperature further. Finally, the crystals were collected and cleaned using a Kimwipe paper.

Experimental setup

The experimental setup consisted of an amplified femtosecond laser system (Light Conversion PHAROS) coupled to an optical parametric amplifier (OPA, Light Conversion ORPHEUS). The laser produces a train of pulses centered at 1028nm with a repetition rate of 3 kHz, pulse duration of 300 fs and a pulse energy of 2 mJ. A small fraction (5%) of the main beam was split off and used as a NIR probe while the main part pumped the OPA producing a MIR pump beam. Pump and probe pulses were spatially and temporally overlapped inside the LHPs. The resulting PL was sampled with an amplified silicon photodetector (PDA-100A2, Thorlabs). A short pass filter (Thorlabs) was used in order to cut off the remaining 1030 nm light. Beam diameters were characterized by the knife-edge technique.

Polarization resolved scans were performed by first converting the linearly polarized MIR radiation from the OPA into a circularly polarized state by means of a tunable quarter-wave plate (ALPHALAS) and a subsequent rotation of the polarization plane by a wiregrid polarizer (THORLABS).

In the two-color experiment a pair of half-wave plate and Glan-Taylor polarizer (GT10, Thorlabs) and a pair of wiregrid polarizers were used to continuously tune the incident power in the 1030 nm and 4500 nm arms respectively.

The PL spectra were taken in reflection geometry by pumping the sample with respective wavelengths at an intensity of $1 \times 10^{11} \text{ W/cm}^2$ and sampling the PL with a fiber coupled spectrometer (OceanOptics FLAME-T).

Calculation of photoluminescence in LHPs

To understand the parametric dependence of the PL, we use the Landau-Dykhne adiabatic approximation where the probability of transition from the initial state i to the

final state f is given by the expression($\hbar = 1$) [34]

$$W_{fi} \sim \exp\left(-2\text{Im} \int_0^T (\mathcal{E}_f(t) - \mathcal{E}_i(t))dt\right), \quad (4)$$

where $\mathcal{E}(t)$ is the instantaneous energy of the time-dependent Hamiltonian, H ; T is the (complex) instance of time when $\mathcal{E}_f(t) = \mathcal{E}_i(t)$. To calculate the energies, we use the following Hamiltonian [16, 21]

$$H = \frac{1}{2} \left(\Delta + t_3 \frac{(\mathbf{k}a)^2}{2} \right) \tau_3 \otimes \sigma_0 + 2ta\tau_2 \otimes \sum_{l=1}^3 \sigma_l k_l, \quad (5)$$

which describes the band structure in the vicinity of the bandgap, i.e., $k \rightarrow 0$. Here, $\Delta \simeq 2.4\text{eV}$ is the energy gap between the conduction and valence bands; $t \simeq 0.6\text{eV}$ and $t_3 \simeq 0.9\text{eV}$ are the hopping integrals; $a \simeq 0.586\text{nm}$ is the lattice spacing; τ_i and σ_i are the Pauli matrices acting on the orbital and quasispin degrees of freedom, respectively. Further details of the used notation can be found in Ref. [22]. Note that we do not include the spin-electric term [23] in our calculations, because its contribution will be subleading for $\omega \rightarrow 0$. External fields enter Eq. (5) via the minimal coupling substitution $\mathbf{k} \rightarrow \mathbf{k} - e\mathbf{A}$; we shall assume weak fields so that $ea\mathbf{A} \rightarrow 0$. We are interested in the regime that is exponentially sensitive to the parameters. Therefore, we shall consider $\mathbf{k} = 0$, which determines the most probable excitation process. With these approximations, the Hamiltonian of interest reads

$$H = \frac{1}{2} \left(\Delta + \frac{t_3(ea\mathbf{A})^2}{2} \right) \tau_3 \otimes \sigma_0 + 2eat\tau_2 \otimes \sum_{l=1}^3 \sigma_l A_l. \quad (6)$$

Its energies are

$$\mathcal{E}_i = -\sqrt{\frac{1}{4} \left(\Delta + \frac{t_3(ea\mathbf{A})^2}{2} \right)^2 + 4t^2(ea\mathbf{A})^2}, \quad (7)$$

and $\mathcal{E}_f = -\mathcal{E}_i$. Note that the energy states are double degenerate. Therefore, in general, we should define a conserved quantity – quasi-spin, and consider separate quasi-spins in parallel. However, as Eq. (4) is independent of this quantum number, we will not take this degeneracy into account. To calculate the value of τ that appears in Eq. (4), we solve the equation $\mathcal{E}_i = 0$, which leads to $(ea\mathbf{A})^2 \simeq -\Delta^2/(\Delta t_3 + 16t^2)$. This expression together with Eqs. (4) and (7) provide the basis for our calculations of PL in the main text.

As an example, let us calculate the PL intensity for a monochromatic light beam. We assume that the vector potential has the form $\mathbf{A} = -\mathbf{E}_{AC} \sin(\omega t)/\omega$, where \mathbf{E}_{AC} is a constant vector that defines the strength of the electric fields (recall that $\mathbf{E} = -\partial\mathbf{A}/\partial t$ in SI units). It is clear that to satisfy $\mathcal{E}_f(t) = \mathcal{E}_i(t)$, t should be imaginary, i.e., $t = i\tau$, where

$$\tau = \frac{1}{\omega} \text{arsinh} \left(\frac{\omega}{eaE_{AC}} \sqrt{\frac{\Delta^2}{\Delta t_3 + 16t^2}} \right). \quad (8)$$

Now, we have all ingredients to calculate W_{fi} :

$$W_{fi} \sim \exp \left(-2\text{Im} \int_0^{i\tau} \left[\Delta + \frac{\Delta t_3 + 16t^2}{2\Delta} (ea\mathbf{A})^2 \right] dt \right),$$

which leads to Eq. (2) of the main text with the Keldysh parameter for our problem

$$\gamma_K = \frac{\omega}{eaE_{AC}} \sqrt{\frac{\Delta^2}{\Delta t_3 + 16t^2}}. \quad (9)$$

PL intensity at strong fields

Let us first consider the situation when n_0 is of the order of A_1/A_2 , but still much smaller than $A_2/A_3 \simeq 10^{18}\text{cm}^{-3}$ [37]. In this case $dn/dt = -A_1n - A_2n^2$, which leads to $n = Ce^{-A_1t}/(1 - A_2Ce^{-A_1t}/A_1)$, where $C = n_0/(1 + A_2n_0/A_1)$. The corresponding PL intensity reads

$$I_{PL} \sim \left(n_0 + \frac{A_1}{A_2} \ln \left[\frac{A_1}{A_1 + A_2n_0} \right] \right). \quad (10)$$

Noticing that $W_{fi} \sim n_0$, this leads to the result presented in the main text: $I_{PL} \sim \alpha W_{fi} - \ln(1 + \alpha W_{fi})$, where α is a fitting parameter. Inclusion of the processes with $i > 2$ in the rate equation will lead to more fitting parameters, and, correspondingly, to a better agreement between the theory and the data. From a physical point of view higher-order processes suppress two-body losses, and effectively renormalize the initial density for the radiative recombination. Phenomenologically, this can be easily included using the following expression $I_{PL} \sim \frac{\alpha W_{fi}}{1 + \beta W_{fi}} - \ln \left(1 + \frac{\alpha W_{fi}}{1 + \beta W_{fi}} \right)$. This expression with two fitting parameters reproduces our data well everywhere.

Supplementary Material for ‘Dynamical Schwinger effect and non-perturbative light detection in lead halide perovskites’

Ionization in the presence of a frozen-in electric field.

Let us assume that the vector potential has the form

$$\mathbf{A} = -\mathbf{E}_{DC}(t - t_i) - \mathbf{E}_{AC} \frac{\sin(\omega t)}{\omega}, \quad (11)$$

where \mathbf{E}_{DC} and \mathbf{E}_{AC} are constant vectors that define the strength of the DC and AC electric fields, respectively; t_i is some constant that is determined by initial conditions. We assume that $\mathbf{A}(t = 0) = 0$, which means that the difference between energy levels at $t = 0$ is Δ . This implies that $t_i = 0$.

It is clear that to satisfy $\mathcal{E}_f(t) = \mathcal{E}_i(t)$, t should be imaginary, i.e., $t = i\tau$, where τ satisfies the equation

$$E_{DC}^2 \tau^2 + 2(\mathbf{E}_{DC} \mathbf{E}_{AC}) \frac{\tau \sinh(\omega \tau)}{\omega} + E_{AC}^2 \frac{\sinh^2(\omega \tau)}{\omega^2} = \frac{\Delta^2}{(ea)^2 (\Delta t_3 + 16t^2)}. \quad (12)$$

We assume that $E_{DC} \rightarrow 0$ so that

$$eaE_{DC}\tau \cos(\theta) + eaE_{AC} \frac{\sinh(\omega \tau)}{\omega} \simeq \sqrt{\frac{\Delta^2}{\Delta t_3 + 16t^2}}, \quad (13)$$

where θ is the angle between \mathbf{E}_{AC} and \mathbf{E}_{DC} . We can solve this equation iteratively. At the first iteration, we neglect the static field completely:

$$eaE_{AC} \frac{\sinh(\omega \tau^0)}{\omega} \simeq \sqrt{\frac{\Delta^2}{\Delta t_3 + 16t^2}} \rightarrow \tau^0 = \frac{1}{\omega} \operatorname{arsinh} \left(\frac{\omega}{eaE_{AC}} \sqrt{\frac{\Delta^2}{\Delta t_3 + 16t^2}} \right). \quad (14)$$

This expression reproduces the result for one-color tunnel ionization. At the second iteration, we derive:

$$\begin{aligned} eaE_{DC}\tau^0 \cos(\theta) + eaE_{AC} \frac{\sinh(\omega \tau^1)}{\omega} &\simeq \sqrt{\frac{\Delta^2}{\Delta t_3 + 16t^2}} \rightarrow \\ \tau^1 &= \frac{1}{\omega} \operatorname{arsinh} \left(\frac{\omega}{eaE_{AC}} \sqrt{\frac{\Delta^2}{\Delta t_3 + 16t^2}} - \frac{E_{DC}}{E_{AC}} \omega \tau^0 \cos(\theta) \right). \end{aligned} \quad (15)$$

We have checked numerically that for $E_{DC} \ll E_{AC}$, τ^1 approximates τ well.

The expression for τ_1 allows us to compute W_{fi} :

$$W_{fi} \sim \exp \left(-2 \operatorname{Im} \int_0^{i\tau^1} \left[\Delta + \frac{\Delta t_3 + 16t^2}{2\Delta} (ea\mathbf{A})^2 \right] dt \right), \quad (16)$$

so that

$$W_{fi} \sim \exp \left(-2\tau^1 \Delta + (eaE_{AC})^2 \frac{\Delta t_3 + 16t^2}{4\Delta} \left[\frac{\sinh(2\omega \tau_1) - 2\omega \tau_1}{\omega^3} + \frac{8E_{DC}}{E_{AC}} \cos(\theta) \frac{\omega \tau_0 \cosh(\omega \tau_0) - \sinh(\omega \tau_0)}{\omega^3} \right] \right), \quad (17)$$

where, for consistency of derivations, we use τ_0 when we multiply by E_{DC} . Note that because the direction of \mathbf{E}_{AC} is defined only up to a phase π , we should use absolute value of $\cos(\theta)$ in the expression.

Additional information for the discussion on frozen-in electric fields

As is mentioned in the main text, the two-fold symmetric polarization dependence in Fig. 2B of the main text appears surprising since the measurement is performed at room temperature where MAPbBr₃ is expected to be in the cubic phase. To further understand this, we approximate the rate of tunneling ionization with the following expression

$$W_{fi} \sim e^{-\frac{5}{3} \frac{\Delta}{eaE} \sqrt{\frac{\Delta^2}{\Delta t_3 + 16t^2}}}, \quad (18)$$

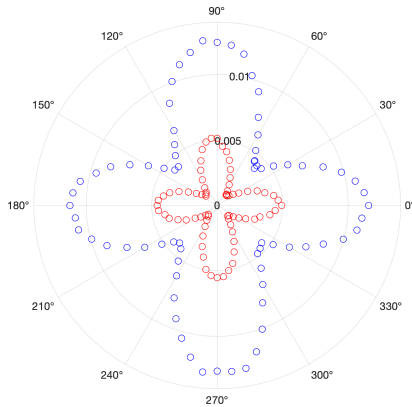


FIG. 4. Polarization scan taken at $eaE_{AC} \simeq 0.284\text{eV}$ (red markers) and $eaE_{AC} \simeq 0.312\text{eV}$ (blue markers). The PL intensity is shown in arbitrary units.

which is valid in an adiabatic regime. We see that there are a few possibilities to change the rate as a function of the angle. For example, either E or t_3 and t can depend on the angle. Let us first assume that E is independent of the angle and that $t \rightarrow t + \delta t$ and $t_3 \rightarrow t_3 + \delta t_3$, where δt and δt_3 determine the change of the hopping integrals. In this case, for the parameters of our system, we derive

$$W_{fi} \sim e^{-1.4 \frac{\Delta}{eaE}} e^{0.5 \frac{\delta}{eaE}}, \quad (19)$$

where $\delta = \delta t_3 + 32t \frac{\delta t}{\Delta} \simeq \delta t_3 + 8\delta t$. Assuming that $\delta t_3 \sim \delta t$, we have $\delta \simeq 10\delta t$. Our data show that for $eaE = 0.140\text{eV}$ the change in PL intensity can be as large as 40, see Fig. 2B of the main text. This means that the change of the hopping coefficient can be $\delta t \simeq 0.05\text{eV}$. Such a change implies that the effective mass is modified by about 10 – 20%, which can be achieved if the intrinsic strains in a single-crystal LHPs are of the order of 0.5% [43]. Depending on the preparation of the LHP single crystal, it can either be strain free or have strains $\simeq 0.1\%$ [44]. We are not aware of a mechanism that can lead to a large renormalization of the effective mass under such weak strains. Therefore, we conclude that the electric field E depends on angle, which leads to the hypothesis of ferroelectric domains presented in the main text.

In Fig. 4 we present a PL scan with a focal spot diameter of $126\mu\text{m}$ ($1/e^2$).

Hysteresis of PL intensity

The samples show limited hysteresis with respect to the intensity scaling. As an example we show the data for MAPbBr₃ obtained at 300K for a pump wavelength of $4\mu\text{m}$. Note that in all our intensity dependent studies care was taken not to exceed values that would lead to substantial hysteresis. For the given example, this would mean an upper limit of $8 \times 10^{14} \text{W}/\text{m}^2$ on the applied intensities.

Abraded samples of MAPbBr₃

As was mentioned above, the efficiency of tunneling ionization is very sensitive to the local properties of the sample (stress, static fields, etc). Indeed, it has been observed that photoluminescence becomes visibly enhanced when the irradiated region happens to be situated near structural defects such as surface inhomogeneities or sample edges/cracks. This is unfortunate for possible infrared imaging applications of dynamical SE in perovskites, as structure-induced variations of PL are going to obscure the intrinsic PL image reflecting the spatial distribution of the irradiating mid-infrared wave-front.

Sample imperfections are unavoidable in practice. Therefore, not being able to ensure sample homogeneity by removing the imperfections one can take the other extreme and instead homogenize the defect distribution, thus obtaining a quasi-uniform sample suitable for infrared-imaging purposes.

Specifically, in this work we mechanically grind the sample by rubbing an intact single crystal of MAPbBr₃ against a fine 1 μm -grit Al₂O₃. As a result, we obtain a sample consisting of a substrate (sandpaper) covered by a powder of

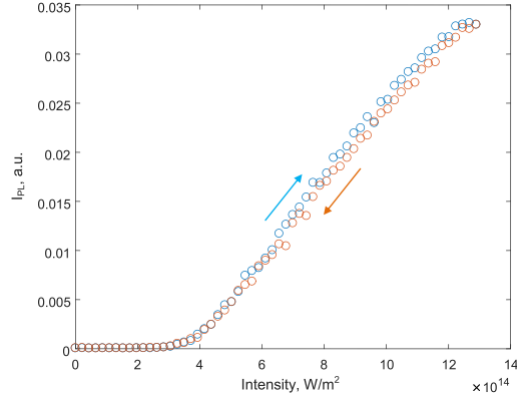


FIG. 5. Hysteresis of the PL intensity for MAPbBr₃ at a pump wavelength of 4 μ m.

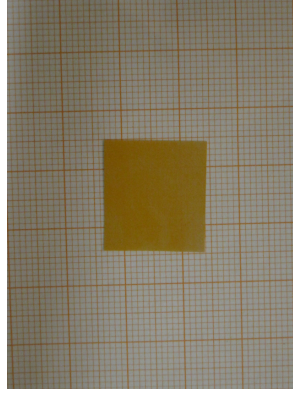


FIG. 6. Abraded sample

perovskite microcrystals as shown in Fig. 6. Our experience shows that microcrystal samples obtained this way are very robust, retaining the ability to PL under infrared-irradiation for years after being manufactured even if stored in atmosphere. The additional advantage of such samples as compared to single-crystal ones is the former being more sensitive than the latter since local stresses as a rule tend to enhance PL efficiency.

To characterize the morphology of the microcrystal comprising the abraded samples, we first cut the sandpaper with microcrystals on top of them into small mm-sized pieces, which were then dropped into hexane and sonicated for 5 minutes. The resulting solution was drop casted on silicon substrates and allowed to dry. In this way prepared microcrystal samples were subsequently imaged by a SEM microscope. The observed grain sizes are shown in Fig. 7. From the evaluation of the grain/particle statistics, we obtain average grain size of about $320 \text{ nm} \pm 60 \text{ nm}$ and a particle size of $1.3 \text{ }\mu\text{m} \pm 0.23 \text{ }\mu\text{m}$.

To investigate cooperation of dynamic fields and AC-biasing, the sample is placed in a defocused 1030 nm beam while being kept in the focus of the 4500 nm pump beam. Images of the resulting PL were taken using a CMOS camera (Point Grey Research PGR-CM3-U3-50S5M-CS).

Photoluminescence from CsPbBr₃

To demonstrate tunnel ionization in another perovskite, we study the PL spectra of CsPbBr₃ irradiated by a 4 μ m laser, see Fig. 8. As for MAPbBr₃, we observe that the PL intensity is exponentially sensitive to the strength of the external electric field. The crucial difference however is that our analytical predictions for MAPbBr₃ do not describe the observed data in CsPbBr₃. This could have been anticipated as in our derivations we relied on the cubic structure of the material. However, CsPbBr₃ (unlike MAPbBr₃) has an orthorhombic structure at room temperature so a more careful analysis must be in order. Further, we note that if the density of charge carriers is small (note that the intensity of the external electric field is relatively small in our experiment with CsPbBr₃), then an electron can recombine only with its partner hole created in the tunnel ionization process or with localized trap states. These

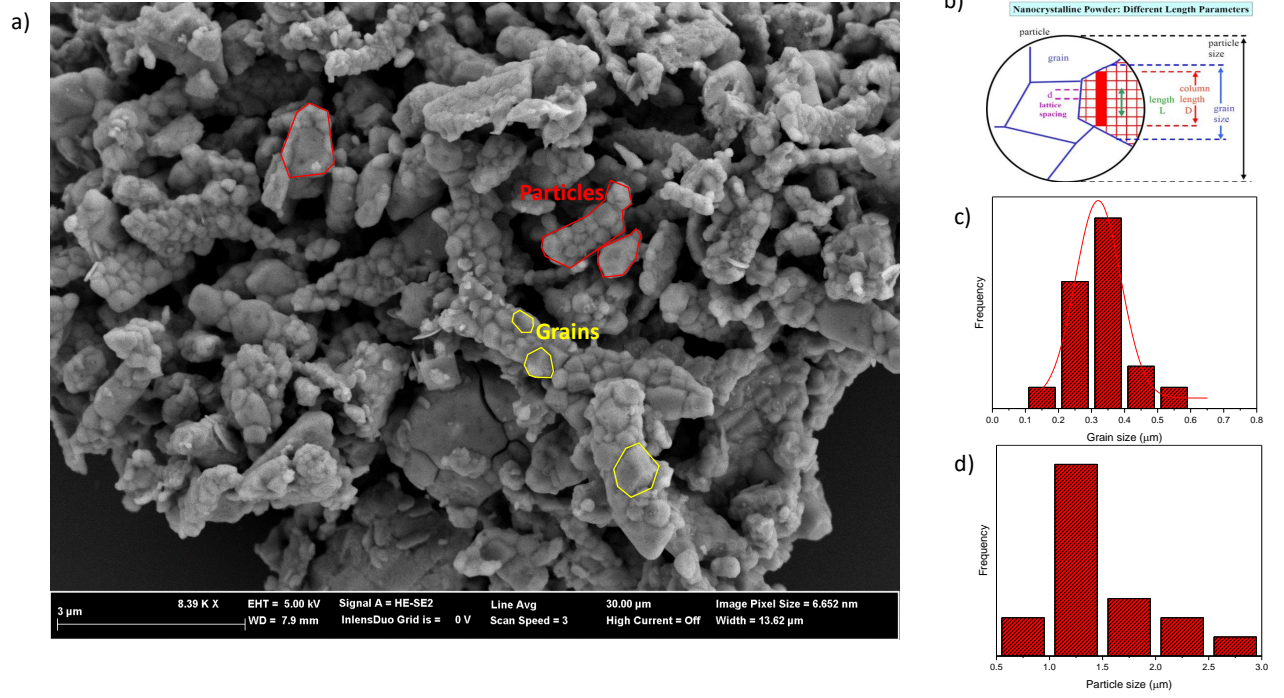


FIG. 7. a) Abraded sample as imaged by a SEM microscope with ‘particles’ and ‘grains’ highlighted in red and yellow, respectively; b) a schematic representation of a grain; c) grain size; d) particle size distributions.

processes are not included in bimolecular radiative recombination used in our analysis of MAPbBr_3 .

To quantify the deviation from the W_{fi}^2 -behavior observed in MAPbBr_3 at small fields, we fit our CsPbBr_3 data with W_{fi}^δ , where δ is a fitting parameter. We find that $\delta \simeq 1.2$ can be used to describe the data. As this value is close to unity, we hypothesize that the radiative processes in CsPbBr_3 for the considered parameters are mainly of monomolecular origin, see also Refs. [30, 52].

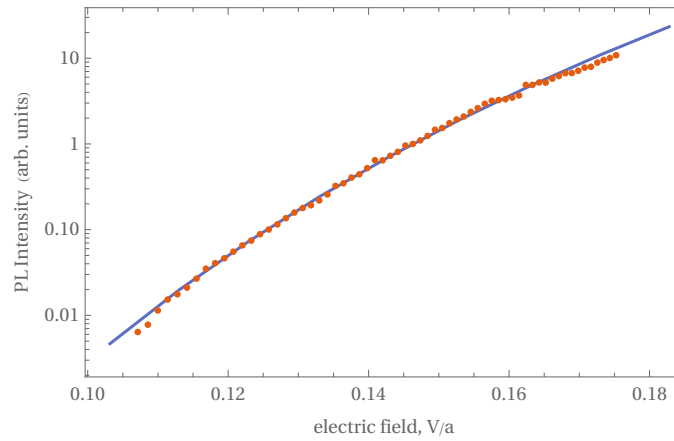


FIG. 8. PL intensity for CsPbBr_3 under $4\mu\text{m}$ pumping (markers). The solid curve demonstrates the functional dependence of $(W_{fi})^{1.2}$.